

Drying of Lithium-Ion Battery Anodes for Use in High-Energy Cells: Influence of Electrode Thickness on Drying Time, Adhesion, and Crack Formation

Jana Kumberg,* Marcus Müller, Ralf Diehm, Sandro Spiegel, Christian Wachsmann, Werner Bauer, Philip Scharfer, and Wilhelm Schabel

When fabricating battery electrodes, their properties are strongly determined by the adjusted drying parameters. This does not only affect their microstructure in terms of adhesion, but also influences cell performance. The reason is found to be the binder transported to the surface during drying. Herein, it is shown that when thicker electrodes are processed, new challenges arise. On the one hand, loss of adhesion associated with certain drying conditions becomes a more serious problem; on the other hand, cracking occurs at a certain drying rate and with increasing electrode thickness.

1. Introduction

To establish electric vehicles as a competitive alternative to internal combustion engine cars, improving consumer acceptance is mandatory. According to the “E-mobility Index 2018” study by Roland Berger, one major disadvantage of lithium-ion battery packs is their limited driving range. Intimately connected with the driving range is the volume of the cell pack and thus the weight of the powertrain.^[1] As an approach to increase energy density and thereby driving range while concurrently saving

costs in terms of inactive material, thicker electrodes may be applied.^[2,3] Their advantage is an improved ratio of active electrode material to inactive components such as the current collector and separator.

In recent studies, the cell performance of thick electrodes has been investigated, showing a loss in capacity at C rates exceeding C/5. This seems to be caused by mass transport limitations of lithium ions in the electrolyte phase and restricted electron transport in the solid phase.^[4–7] Research therefore focuses on the structuring of electrodes, e.g., by laser post-processing steps or by new processing methods to provide pathways from the electrode surface to the substrate for faster Li-ion transport.^[8–11] Though a broad knowledge base about transport limitations and tailoring of electrode porosity exists, the significant influence of the electrode production process, namely speaking of the coating and drying conditions on electrode microstructure and cell performance, is often not considered.^[10,12–15]

The mechanism of electrode drying according to latest knowledge is summarized in Figure 1.^[16] Directly after coating and before the drying step starts, the wet film has a homogeneous particle and additive distribution within the solvent (Figure 1a). With the wet film entering the dryer, the solvent evaporates from the surface at a defined mass flow of the evaporating solvent, called drying rate, \dot{m}_S . The film starts to shrink according to Equation (1) with a rate of evaporation equaling that of a pure water film.

The mechanism of electrode drying according to latest knowledge is summarized in Figure 1.^[16]

Directly after coating and before the drying step starts, the wet film has a homogeneous particle and additive distribution within the solvent (Figure 1a). With the wet film entering the dryer, the solvent evaporates from the surface at a defined mass flow of the evaporating solvent, called drying rate, \dot{m}_S . The film starts to shrink according to Equation (1) with a rate of evaporation equaling that of a pure water film.

$$\dot{m}_S = \tilde{M}_S \tilde{\rho}_G \beta_{S,G} \ln \frac{(1 - \tilde{y}_{S,\infty})}{(1 - \tilde{y}_{S,Ph})} \quad (1)$$

The drying rate depends on the molar mass of the solvent \tilde{M}_S , the molar density of the surrounding gas flow $\tilde{\rho}_G$, the molar fraction of solvent in the drying air $\tilde{y}_{S,\infty}$, and the molar fraction of the solvent at the solvent–gas interface $\tilde{y}_{S,Ph}$. The molar fractions as well as the density depend on the drying temperature. This is also true for the mass transfer coefficient $\beta_{S,G}$, which is usually defined as the diffusion coefficient of the solvent within the surrounding phase throughout the boundary layer. The mass transfer coefficient β can also be determined by the Lewis analogy. Heat and mass transfer coefficient α and β are connected by a dependency on the heat capacity of the gas $c_{p,G}$, the molar density of the gas ρ_G , the Lewis

J. Kumberg, R. Diehm, S. Spiegel, C. Wachsmann, Dr. P. Scharfer, Prof. Dr. W. Schabel
Institute of Thermal Process Engineering (TVT)
Thin Film Technology (TFT)
Karlsruhe Institute of Technology (KIT)
Straße am Forum 7, D-76131 Karlsruhe, Germany
E-mail: jana.kumberg@kit.edu

Dr. M. Müller, Dr. W. Bauer
Institute of Applied Materials – Energy Storage Systems (ESS)
Karlsruhe Institute of Technology (KIT)
Hermann-von-Helmholtz-Platz 1, 76144 Eggenstein-Leopoldshafen, Germany

 The ORCID identification number(s) for the author(s) of this article can be found under <https://doi.org/10.1002/ente.201900722>.

© 2019 The Authors. Published by WILEY-VCH Verlag GmbH & Co. KGaA, Weinheim. This is an open access article under the terms of the Creative Commons Attribution License, which permits use, distribution and reproduction in any medium, provided the original work is properly cited.

The copyright line for this article was changed on 30 November 2020 after original online publication.

Correction added on 30 November 2020, after first online publication: Projekt Deal funding statement has been added.

DOI: 10.1002/ente.201900722

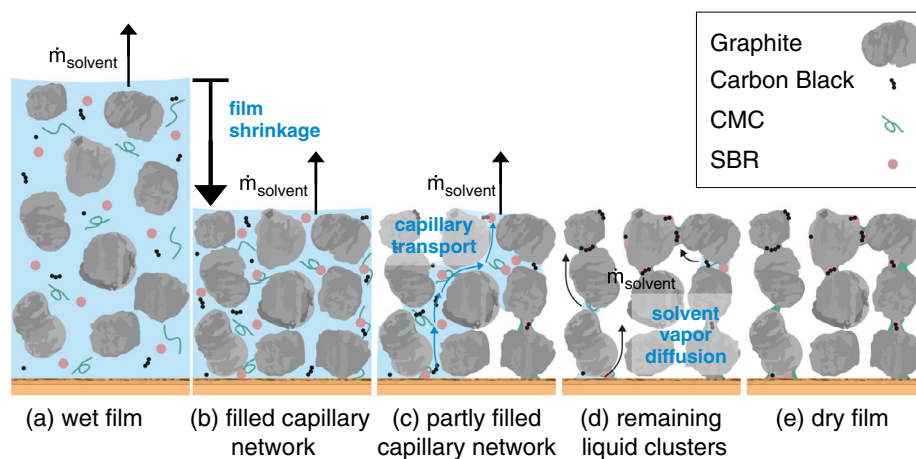


Figure 1. Schematic of the drying process of a particulate coating with the initial wet film before drying starts a) until all solvent has been removed and e) the dry film is left. b) At the beginning, the film shrinks and solvent evaporates from the surface until the final porosity is reached. c) The water-filled network empties due to capillary transport of liquid to the film surface. d) If liquid clusters remain within the structure, they evaporate within the structure and diffuse to the surface.

number (Le), and the flow conditions with $n = \frac{1}{3}$ for laminar flows and $n = 0.4$ for turbulent flows according to Equation (2).^[17]

$$\frac{\alpha}{\beta} = c_{p,G} \tilde{\rho}_G Le^{1-n} \quad (2)$$

The heat transfer coefficient in itself is defined by the dryer dimensions and the air flow and can thus be determined characteristically for each dryer.^[17,18]

With ongoing evaporation and as the wet film's height decreases, particles move closer together until they reach the final porosity and the film cannot shrink any more. A capillary network with solvent-filled capillaries is developed (Figure 1b). As shown in Figure 1c, even after the end of film shrinkage, the solvent will evaporate at the film surface and the constant drying rate prevails. The reason is the capillary network, where small pores remain filled with solvent within the microstructure leading to the film surface. These smaller pores maintain a high evaporation rate at the film surface at the cost of bigger pores being emptied within the porous structure, reaching even the interface between the substrate and particles at the bottom of the film.

There is the possibility of remaining liquid clusters within the structure that are not accessible for capillary transport. These liquid clusters will have to evaporate within the porous structure and therefore have to overcome an additional transport resistance, which reduces the drying rate. The mass transfer coefficient in Equation (1) is replaced by a decreased mass transfer coefficient that includes the additional mass transport resistance due to diffusion through the porosity.^[19–21]

Research on the drying behavior of state-of-the-art electrodes from *N*-methyl-2-pyrrolidone (NMP)-based slurries using polyvinylidene fluoride (PVDF) as the binder has found that the drying of these electrodes is dominated by a distinct constant rate period. A constant evaporation rate prevails even after the film stops shrinking and the surface is not necessarily saturated with the solvent.^[15]

This means, there is no diffusional limitation for solvent transport within the porous electrode, reducing the drying rate after the end of film shrinkage, which can be explained by capillary transport of solvent to the electrode surface. However, it could also be shown that for electrodes with state-of-the-art thickness of about 60 μm , some liquid clusters remain within the electrodes' microstructure, which have not been emptied by capillary transport and thus have to evaporate on site and move through the inner pore structure, not in the liquid phase but in the gaseous phase during the drying process.^[16] The number of liquid clusters though seems to be negligible for state-of-the-art electrodes, since it is not reflected in the drying curve that is still governed by a constant drying rate.

Regarding the impact of the drying mechanism on the additive distribution, some research exists as well.

A recent publication using a time-resolved Cryo-scanning electron microscopy (SEM) measurement technique combined with energy-dispersive X-ray spectroscopy (EDS) shows for NMP-based anodes that for state-of-the-art electrode thicknesses, solvent-filled pores can be found throughout the microstructure. These pores lie directly next to empty pores at the substrate–particle interface. These findings confirm the assumption of capillary forces governing the drying process after the end of film shrinkage. In addition, EDS was used to track the evolving distribution of the binder during the drying process, showing its accumulation on the film surface during capillary transport. Hypothesis is that additives are dragged along with the solvent through the capillaries to the surface, which seems to be the case for carbon black as well as for the binder.^[16,22] In further investigations, a correlation between drying velocity, electrode adhesion on the substrate, and cell performance has been proven, indicating that high drying velocities lead to a depletion of binder at the interface between the substrate and active material. This results in a loss of adhesion and has also been found to lead to a loss in cell capacity.^[15,23,24] The binder gradient which is correlated with certain drying temperatures and the resulting loss in cell capacity has been further illuminated by means of

impedance spectroscopy.^[25] The mechanisms of how capillary forces seem to transport the solvent and binder to the electrode surface during the drying process while higher drying rates allow less time for compensation of developing binder concentration gradients by back diffusion have been confirmed in simulations.^[26] These findings are also in good agreement with results showing that higher drying temperatures at a certain drying rate are actually beneficial for microstructure homogeneity.^[24]

When going to thicker electrodes, experiments on binder migration during the drying process have been undertaken with electrodes of thicknesses of up to 450 μm using SEM/EDS measurements to detect a pronounced binder content at the electrode surface especially for thick electrodes dried at high drying velocities.^[27] In research regarding the improvement of high-energy electrodes, the influence of the actual processing step, strictly the drying process, is usually neglected.

This research focuses on the interrelationship between controlled drying conditions and their influence on the microstructure of thick electrodes. Binder migration evaluated by adhesion force measurements as well as the tendency for cracking during the drying process is investigated. The aim is not the characterization of the drying behavior of the slurry given here, as absolute adhesion forces as well as cracking thickness will be different for other slurry compositions or materials, but to illuminate the relationship between controlled drying conditions and the aptitude for binder to migrate as well as for film cracking.

2. Results and Discussion

Drying experiments were conducted with water-based slurries, consisting of graphite, carbon black, and the binder system carboxymethyl cellulose (CMC) and styrene-butadiene rubber (SBR). For the drying step, a periodically moving heating plate and a slot nozzle dryer were used and isothermal drying conditions were adjusted. The isothermal drying temperature was calculated to fit a certain drying rate at a certain air flow rate and dew point of the drying air, thus equaling the steady-state temperature of an industrial dryer under the same drying conditions. More details are given in the Experimental Section.

2.1. Drying Curves

Drying curves of water-based slurries with 43wt% graphite were taken and the drying behavior of these electrodes was investigated. The drying curves were determined by means of residual moisture measurements at different time intervals during the drying step. More details are given in the Experimental Section. The aim was a comparison of the drying characteristics of electrodes with increasing area weights. As shown in **Figure 2**, the microstructure of a real electrode strongly deviates from the simplified model introduced in Figure 1. The active material particles vary in size and shape, leading to a broad and inhomogeneous pore radii distribution. As explained earlier, the drying process is dominated by this pore radii distribution, especially after the end of film shrinkage. From that point on during drying, a well-connected capillary liquid network is mandatory for liquid evaporation to take place at the film surface and a prevailing constant drying rate that is not influenced by diffusional resistance

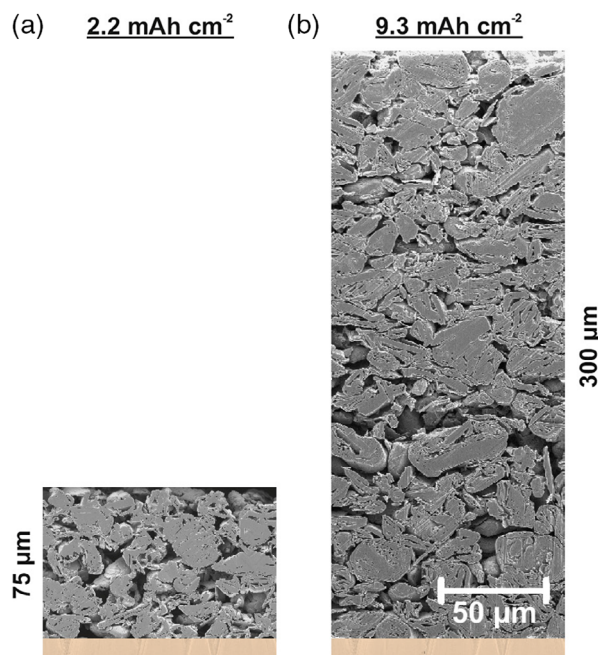


Figure 2. SEM pictures of two electrodes that differ in their film height. A state-of-the-art electrode with a thickness of 75 μm (left) is compared with a thick electrode of 300 μm (right).

within the pore network. While this might be true for thin electrodes, hypothesis is that this is not the case when thick electrodes are dried, due to the complexity of the capillary network that gains importance for thicker electrodes. The drying behavior of thin and thick electrodes is investigated and results are shown in **Figure 3**.

Drying curves of electrodes of four different loadings are given, depicting the decreasing solvent loading over drying time at a defined drying rate of $0.75 \text{ g m}^{-2} \text{ s}^{-1}$. The experimental data are compared to a simulation assuming gas-phase

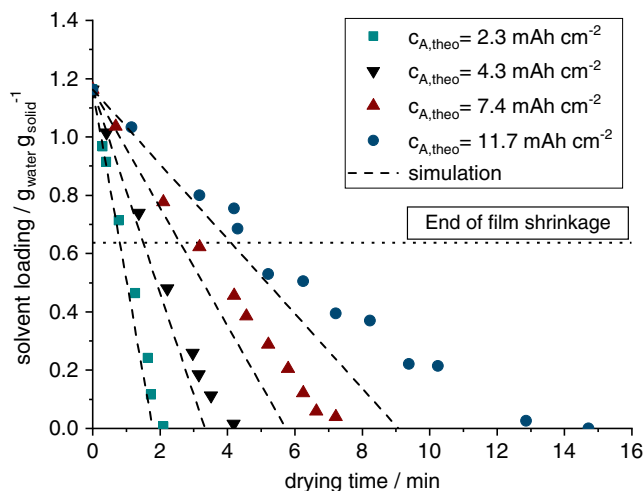


Figure 3. Comparison of experimental data and simulation for gas-phase drying kinetics of electrodes, possessing different theoretical capacities and electrode thicknesses, respectively.

controlled drying kinetics. The heat transfer coefficient was $\alpha = 35 \text{ W m}^{-2} \text{ K}^{-1}$ and the corresponding mass transfer coefficient $\beta = 0.034 \text{ m}^2 \text{ s}^{-1}$. For the state-of-the-art area capacity of 2.3 mAh cm^{-2} , calculation and experiment are in good agreement and both sum up to a total drying time of about 2 min, starting at 43 wt% solid content. Experiments with higher loadings also show a constant drying rate that prevails beyond the end of film shrinkage, which clearly speaks for capillary transport of solvent to the surface. At the end of the drying time, an increased deviation from theoretical calculations can be observed for all thicker electrodes. This suggests that with increased electrode thickness, the solvent-filled pore network is no longer able to transport all the liquid to the film surface by capillary transport. As a consequence, some liquid clusters remain within the microstructure. The drying rate of this remaining solvent is dependent on the mass transfer coefficient, as well as on solvent vapor diffusion through the microstructure, with the slowest mechanism governing the velocity of the whole process. The porosity functions as a resistance for mass transport. Due to this limitation, the drying rate might decrease at the end of the drying process of thick electrodes.

2.2. Adhesion Force of Thick Electrodes

Adhesion force and drying mechanism are closely related, but due to the complex microstructure not easily predicted by simulation (see Figure 2), the effect of increased area weight and theoretical area capacity on the adhesion force of water-based anodes is experimentally investigated. The results are shown in Figure 4.

As explained in the experimental details, electrodes of different area weights were processed. Drying conditions were kept constant at a drying rate of $0.75 \text{ g m}^{-2} \text{ s}^{-1}$ with a heat transfer coefficient of $35 \text{ W m}^{-2} \text{ K}^{-1}$. The adhesion force between the substrate and electrode was measured using a 90° peel test. Adhesion force is normalized on the adhesion force of 16.2 N m^{-1} of an electrode with a theoretical capacity of 2.2 mAh m^{-2} .

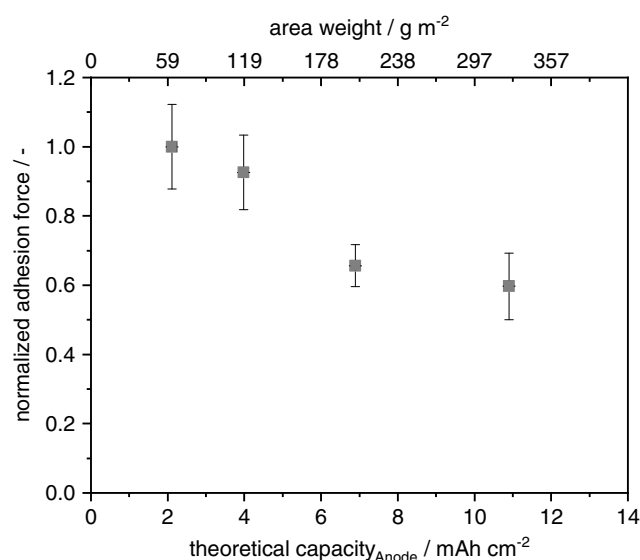


Figure 4. Influence of increased theoretical capacity or area weight on adhesion force for electrodes dried under identical drying conditions.

Adhesion force measurements show a clear trend of decreasing adhesion force when area loading increases.

Results indicate that loss of adhesion force is a problem, when thicker electrodes are to be processed compared with thinner electrodes at identical processing conditions. As explained in some more detail in the next chapter the reason for a loss of adhesion at higher capacities could be due to the length of diffusional pathways. A binder concentration gradient evolving during the drying process as a consequence of capillary transport of solvent and additives to the film surface could be compensated to some extent by back diffusion of binder if the drying time is sufficiently long. When film thickness increases, binder needs more time for a diffusional compensation within the complex network as compared with thin electrodes with shorter pathways from top to bottom.

2.3. Adhesion in Dependency of Drying Rate

As the drying step has a strong impact on the electrode microstructure, a detailed comparison of different drying parameters for thin ($c_{\text{Anode,theo}} = 2.5 \text{ mAh cm}^{-2}$) and thick ($c_{\text{Anode,theo}} = 12.5 \text{ mAh cm}^{-2}$) electrodes is shown in Figure 5. Drying temperature and heat transfer coefficient are adjusted independently as described in the Experimental Section, to separate their particular impact. In Figure 5, electrodes dried at two different drying rates of $1.5 \text{ g m}^{-2} \text{ s}^{-1}$ and $2.5 \text{ g m}^{-2} \text{ s}^{-1}$ are compared. These are obtained by adjusting the air flow, which results in a heat transfer coefficient of either 35 or $80 \text{ W m}^{-2} \text{ K}^{-1}$. In dependency of airflow conditions and dew point, the isothermal drying temperature is determined and adjusted, to obtain the required drying rate. All experimental settings are summarized in Table 1.

The higher heat transfer coefficient of $80 \text{ W m}^{-2} \text{ K}^{-1}$ leads to lower adhesion at both drying rates compared here, which is true for thin and thick electrodes. Adhesion force is normalized on the adhesion force of 18.2 N m^{-1} of an electrode of 2.5 mAh cm^{-2} theoretical area capacity, dried at a theoretical drying rate of $0.75 \text{ g m}^{-2} \text{ s}^{-1}$.

Lower adhesion is not only caused by the higher heat transfer coefficient though, as temperature also has to be adjusted to gain a certain drying rate, as shown in Table 1. The difference in isothermal drying temperature at the same drying rate of $1.5 \text{ g m}^{-2} \text{ s}^{-1}$ but at two heat transfer coefficients is 10°C . This means that a higher temperature benefits adhesion at one drying rate. When two different drying rates at identical isothermal drying temperatures are compared though, adhesion is worse for electrodes dried at higher drying rates.

These findings confirm the assumption that binder back-diffusion processes might take place. At higher drying rates, less time is available for diffusion to balance binder concentration differences caused by capillary pore emptying to some extent. Higher drying temperatures at one drying rate increase the diffusion coefficient and decrease the viscosity of the surrounding solvent, leading to an increased binder mobility. A higher temperature might therefore have a positive effect on adhesion.

Because adhesion of thick electrodes is very much influenced by drying rate and especially by heat transfer coefficients as shown here, it can be assumed that the main drying mechanism

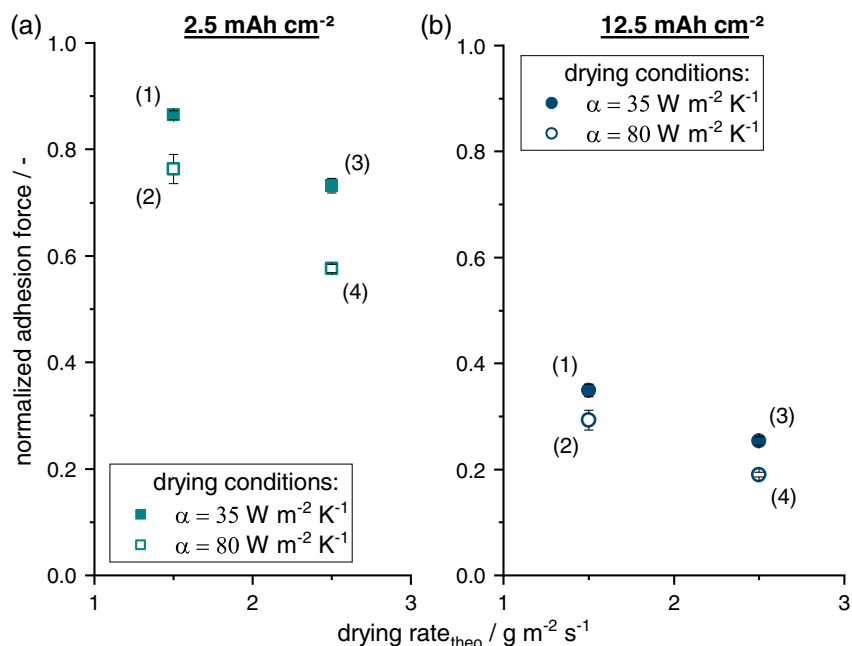


Figure 5. Influence of drying conditions on adhesion force of a) thin and b) thick anodes with a theoretical area capacity of 2.5 and 12.5 mAh cm⁻², respectively. Differentiation between influence of drying rate, heat transfer coefficient, and drying temperature with detailed conditions (1)–(4) depicted in Table 1.

Table 1. Drying conditions of electrodes given in Figure 5.

Setting	Drying rate [g m ⁻² s ⁻¹]	Heat transfer coefficient [W m ⁻² K ⁻¹]	Isothermal drying temperature [°C]
(1)	1.5	35	41
(2)	1.5	80	31
(3)	2.5	35	49
(4)	2.5	80	41

is still capillary transport and not the diffusion of gaseous solvent through the porous microstructure. As diffusional drying kinetics would not lead to mass flows able to drag the binder along to the same extent the capillary transport is, it can be concluded that, even though thick electrodes partly do not dry by capillary transport, considering the results of drying curves shown in Figure 3, this mechanism still dominates the drying behavior of thick electrodes and thereby determines their microstructure.

Results shown here for thin electrodes were also found by Baunach et al. for NMP-based systems.^[24]

Since a lower heat transfer coefficient and a higher drying temperature always accompany each other when a certain drying rate is to be adjusted, one might also assume that temperature influence is not that of a binder concentration compensation by diffusion but a totally different mechanism, namely that of binder being annealed. To discern the impact of annealing and drying, electrodes were dried at 0.75 g m⁻² s⁻¹ and α = 80 W m⁻² K⁻¹ and annealed for 10 min at different temperatures. The results are shown in Figure 6.

Adhesion force is normalized on the adhesion force of 18.9 N m⁻¹ of an electrode prior to annealing.

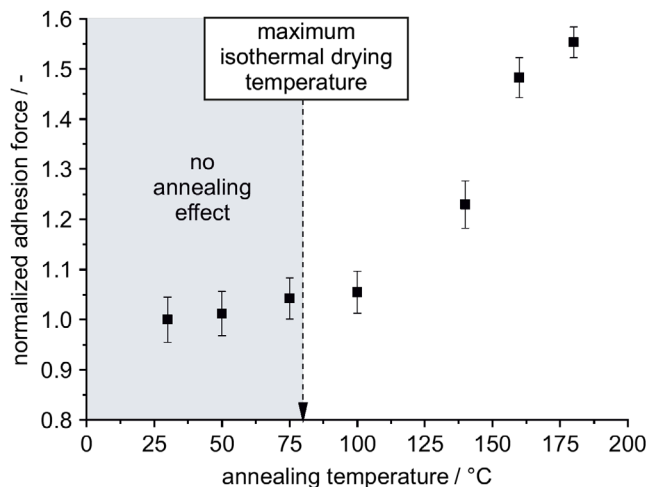


Figure 6. Influence of a post-annealing step at different temperatures on adhesion force. The temperature range at which the drying step takes place with the maximum isothermal drying temperature of 80 °C used in experiments here is compared with the temperature range at which annealing takes place.

Evidently, annealing does have a significant influence on adhesion and is therefore recommended as a post-processing step. However, a prominent increase in adhesion can only be observed at annealing temperatures beyond 100 °C. A slight increase in adhesion of about 1% can be detected when annealing at a temperature of 50 °C. The adhesion difference of a thin electrode dried at 31 °C compared with 41 °C at a drying rate of 1.5 g m⁻² s⁻¹ sums up to about 10% and thereby exceeds the

influence of annealing. As isothermal drying temperature never exceeded 80 °C in this work, it can be concluded that better adhesion at higher temperatures is not caused by annealing but by another mechanism like binder diffusion as proposed.

In **Figure 7**, the findings for the drying behavior of thin and thick electrodes are summarized for different drying rates. The drying rate is varied between 0.75 and 15.5 g m⁻² s⁻¹ for two different heat transfer coefficients (35 and 80 W m⁻² K⁻¹) and the resulting adhesion force is measured.

Adhesion force of electrodes dried with an approximate drying rate of 0.01 g m⁻² s⁻¹ is included in the graph as a colored upper limit of adhesion for low and high area capacity each, which was realized by a drying process under free convection with an estimated heat transfer coefficient of 2.2 W m⁻² K⁻¹ under ambient conditions with a dew point of 15 °C.

Adhesion force is normalized on the adhesion force of an electrode on Cu foil 1 (f1), resulting in an adhesion force of 18.2 N m⁻¹. Further measurements were conducted on Cu foil 2 (f2) under same conditions apart from substrate variation, resulting in an adhesion of 9.7 N m⁻¹. Both electrodes had a theoretical capacity of 2.5 mAh m⁻² and were dried at a theoretical drying rate of 0.75 g m⁻² s⁻¹ and a heat transfer coefficient of 35 W m⁻² K⁻¹. Dry electrodes had 3.73 wt% SBR binder. A higher adhesion when drying at free convection results for both, thin and thick electrodes, compared with electrodes dried at still relatively low drying rates of 0.75 g m⁻² s⁻¹, with a difference in adhesion of about 40%. These findings underline the assumption that a very slow drying process at free convection allows diffusional compensation of binder gradients, which develop due to capillary transport. The adhesion gap between thin and thick electrodes though cannot be overcome by a drying process under free convection.

As slow drying rates are beneficial in terms of adhesion, but lead to high drying times and dryer length, as shown in **Table 2**, drying rate is increased and the impact on adhesion determined. For a slurry of 43 wt% solid content, drying time is calculated under the assumption that only gas-phase kinetics governs the

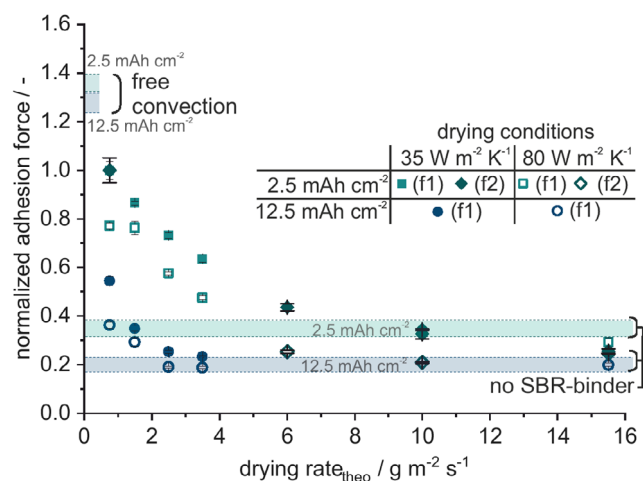


Figure 7. Influence of drying rate on the adhesion force of anodes of a theoretical area capacity of 2.5 mAh cm⁻² compared with anodes of a theoretical area capacity of 12.5 mAh cm⁻² with f1 being Cu foil 1 and f2 being Cu foil 2, resulting in different absolute adhesion forces.

Table 2. Theoretical drying time and corresponding dryer length for a web velocity of 50 m min⁻¹, a slurry of 43 wt% solid content, and an electrode of 2.5 mAh cm⁻² area capacity at different drying rates with the assumption of solely gas-phase-controlled drying kinetics.

Drying rate [g m ⁻² s ⁻¹]	Drying time [s]	Dryer length [m]
0.01	9809	8174.4
0.75	131	109
1.5	65	54.5
3	33	27.2
6	16	13.6
15.5	6	5.3

drying process. As thicker electrodes dry to some extent with a limited drying rate as shown in **Figure 3**, the calculation is limited to state-of-the-art electrodes with 2.5 mAh cm⁻². A drying rate of 1.5 g m⁻² s⁻¹ leads to a drying time of about 1 min and a dryer length of 54.5 m when drying is kept constant in all drying zones. An increase to 3 g m⁻² s⁻¹ allows for drying times of close to half a minute with a dryer length of 27.2 m. From **Figure 5a** decrease in adhesion force of about 25% can be derived at that drying rate with a heat transfer coefficient of 35 W m⁻² K⁻¹, compared with the drying rate of 0.75 g m⁻² s⁻¹.

When the drying rate is further increased up to 15.5 g m⁻² s⁻¹, there is a clear trend to very low adhesion forces converging toward an adhesion force that is achieved when slurries without any SBR binders are processed. The adhesion force of the corresponding electrodes is included in the graph as a colored area and might be a lower limit for electrodes dried with 3.73 wt% SBR binder under very high drying rates. There is also a considerable influence of the heat transfer coefficient. All electrodes dried at one drying rate but at a higher heat transfer coefficient of 80 W m⁻² K⁻¹ show a clear tendency toward a lower adhesion force, compared with electrodes dried with a heat transfer coefficient of 35 W m⁻² K⁻¹.

In summary, it might be deduced that above a certain drying rate, almost no SBR binder remains at the interface between active material and current collector foil. Still it can be said that for state-of-the-art electrodes the drying rate can be increased to a drying rate of 3 g m⁻² s⁻¹, equaling a drying time of 33 s with only 25% loss of adhesion compared with an electrode dried four times more slowly. Also by the utilization of multistage drying profiles binder migration might be reduced to some extent while drying time can be increased.^[28] As the objective here is to illuminate the interrelationship between single process parameters and electrode properties, this is not further investigated.

2.4. CMC Concentration in Dependency of Drying Rate

Processing of the slurry without any CMC, as was done with the SBR binder, is not possible, due to its ability to stabilize the suspension. Because of that, another method was used to get an impression of how drying conditions affect the distribution of CMC within the electrode. Two electrodes were dried at different drying conditions: at a low drying rate of 0.75 g m⁻² s⁻¹ and at a

fast drying rate of $6 \text{ g m}^{-2} \text{ s}^{-1}$. For both electrodes, the substrate was peeled off and the exposed surface was analyzed by EDS. Sodium was used as a marker for the presence of CMC (Na-CMC). Although the setup is not ideal for quantification it was possible to identify differences in the Na distribution between electrode surface (“top”) and the interface to the current collector (“bottom”) in dependence of the drying conditions, as shown in Table 3. For the slowly dried electrode, the Na content at the top and bottom is similar, with 0.26 at% at the top and 0.29 at% at the bottom. The fast-dried electrode shows a deviation of the Na content between top and bottom with 0.39 at% at the top and 0.19 at% at the bottom. The difference in the Na signal between the two drying rates indicates that CMC, same as SBR, accumulates at the surface of the electrode at high drying rates. The loss of adhesion seems therefore always to be affected by migration of both additives SBR and CMC.

2.5. Cracking Behavior Associated with the Drying Rate

The drying process of thick electrodes is not only a challenge because of adhesion loss, but also because of a higher probability for cracking. Because of that, the interrelationship between drying parameters and cracks occurring during the drying step was investigated. Thick electrodes in particular show a tendency for cracking when mechanically stressed or bent; this is not part of this study though. In this work, electrodes were coated with an inclined doctor blade, resulting in dry films with a thickness of $89 \mu\text{m}$ on one side, corresponding to a theoretical capacity of 2.6 mAh cm^{-2} , and a thickness of $512 \mu\text{m}$ on the other side, equaling a theoretical area capacity of 15.1 mAh cm^{-2} . The coating width was 100 mm . Drying conditions were varied between 0.75 and $15 \text{ g m}^{-2} \text{ s}^{-1}$. The hypothesis is that in experiments using an inclined doctor blade, a variation of drying conditions affects the thickness at which cracking occurs which then correlates with different positions where cracks can be detected. In the literature, a dependency between film thickness and critical stress for cracking is given, with a higher tendency for cracking when film thickness is increased.^[29,30] These findings though are influenced by many factors such as particle size, particle size distribution, or binder properties and cannot easily be predicted for a complex system like the one investigated here. Thus, in the following, the interrelationship between drying conditions and tendency for cracking is experimentally examined. In Figure 8, surfaces of four electrodes are pictured that differ in thickness and drying rate, though all of them were dried with a heat transfer coefficient of $80 \text{ W m}^{-2} \text{ K}^{-1}$.

In Figure 8a, an inclined electrode layer is shown with a gradient in thickness reaching from $89 \mu\text{m}$ at the bottom of

Table 3. Binder content at the top and bottom for two differently dried electrodes.

Position	Drying rate [$\text{g m}^{-2} \text{ s}^{-1}$]	Sodium content [at%]
Top	0.75	0.26
Bottom	0.75	0.29
Top	6	0.39
Bottom	6	0.19

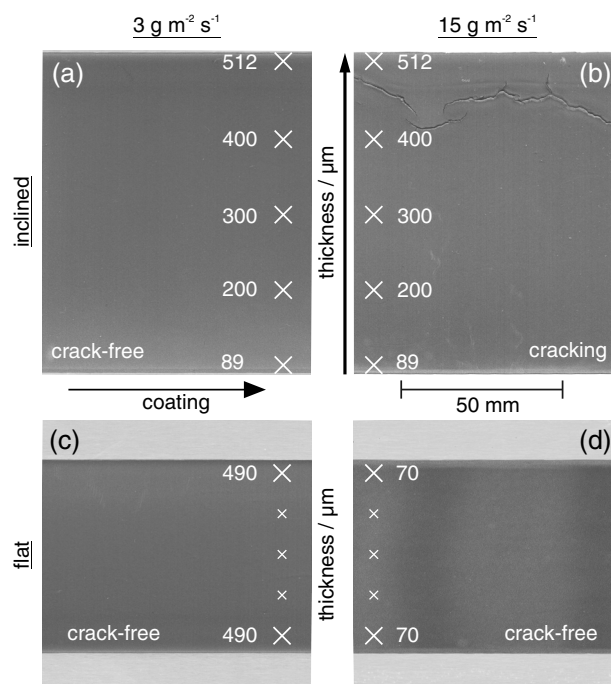


Figure 8. Top view of four different electrodes dried with a heat transfer coefficient of $80 \text{ W m}^{-2} \text{ K}^{-1}$. Electrodes a) and b) are both inclined layers with a thickness reaching from 89 and $512 \mu\text{m}$ each. The electrodes c) and d) are flat without any inclination, with (c) being a flat layer of $490 \mu\text{m}$ thickness and (d) of $70 \mu\text{m}$. Electrode (a) and (c) were dried at a drying rate of $3 \text{ g m}^{-2} \text{ s}^{-1}$ and electrode (b) and (d) were dried at $15 \text{ g m}^{-2} \text{ s}^{-1}$.

the picture to $512 \mu\text{m}$ at the top of the picture. The electrode shown here was dried at a drying rate of $3 \text{ g m}^{-2} \text{ s}^{-1}$ and does not show any cracks at any position or corresponding layer thickness. In contrast in Figure 8b an exemplary electrode of identical inclination but dried at a drying rate of $15 \text{ g m}^{-2} \text{ s}^{-1}$ is shown. Cracks can be identified, starting at a thickness of approximately $400 \mu\text{m}$, with a more detailed evaluation shown in Figure 9. To guarantee that the inclined setup does not influence crack formation, a flat electrode with a thickness of $490 \mu\text{m}$ and a corresponding theoretical area capacity of 14.4 mAh cm^{-2} was dried under the same drying conditions of $3 \text{ g m}^{-2} \text{ s}^{-1}$ with a heat transfer coefficient of $80 \text{ W m}^{-2} \text{ K}^{-1}$. This electrode is shown in Figure 8c and is free of cracks as well.

In Figure 8d a flat electrode with a thickness of $70 \mu\text{m}$ is shown that has been dried under a drying rate of $15 \text{ g m}^{-2} \text{ s}^{-1}$. The layer is again crack free. As shown from the inclined electrode in Figure 8b, the thickness of $70 \mu\text{m}$ of electrode (Figure 8d) at the given drying rate is clearly below the critical crack thickness and thus the pictured electrode does not show any sign of cracking. What can be observed though are two differently shaded areas in the coating direction. This can be detected over the whole electrode length, with gaps in between the patterns corresponding to the slot nozzle distances. It can be assumed that this shading is due to the very short drying time of approximately 6 s , where the electrode position in relation to nozzle position leads to locally strongly increased heat transfer coefficients and thus locally different drying behaviors.

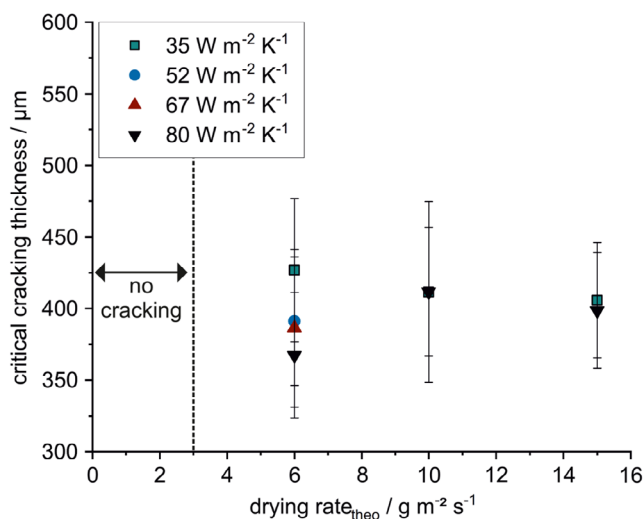


Figure 9. Influence of drying conditions on critical cracking thickness. All anodes were coated with an inclination reaching from 89 and 512 μm in the dry film. Electrodes dried at a drying rate of $6 \text{ g m}^{-2} \text{ s}^{-1}$ showed cracking at film thicknesses exceeding $325 \mu\text{m}$.

To illuminate the relationship between drying rate and cracking thickness in detail, further experiments with inclined layers were conducted and more drying rates were taken into account. All cracks that developed at different drying conditions were analyzed and the corresponding film thickness was determined. The results are shown in Figure 9.

For a drying rate of $3 \text{ g m}^{-2} \text{ s}^{-1}$ or less, independent of heat transfer coefficient, no cracking occurred. When the drying rate was increased to $6, 10,$ and $15 \text{ g m}^{-2} \text{ s}^{-1}$, cracks could be observed. As shown in Figure 9 though, the critical cracking thickness does not seem to decrease when drying rate is increased. However, there seems to be a relationship between minimal cracking thickness and heat transfer coefficient, with a tendency for a lower critical thickness at a higher heat transfer coefficient at the drying rate of $6 \text{ g m}^{-2} \text{ s}^{-1}$. This trend though is not reflected at higher drying rates of 10 and $15 \text{ g m}^{-2} \text{ s}^{-1}$.

A prominent impact of an increasing drying rate can be observed in the overall cracking area as shown in Figure 10.

The percentage of cracking area in relation to the whole electrode area is compared at different drying rates and heat transfer coefficients. Again, electrodes dried at a drying rate of $3 \text{ g m}^{-2} \text{ s}^{-1}$ or less do not show any cracks. The ones dried at $6 \text{ g m}^{-2} \text{ s}^{-1}$ result in about 0.2% crack area with a tendency to an increasing crack area at higher heat transfer coefficients. This trend can also be found for the coatings dried at 10 and $15 \text{ g m}^{-2} \text{ s}^{-1}$. The crack amount increases with the drying rate up to 1% cracking area at a drying rate of $15 \text{ g m}^{-2} \text{ s}^{-1}$ and a heat transfer coefficient of $80 \text{ W m}^{-2} \text{ K}^{-1}$. These experiments show that cracking is influenced by drying conditions, though not as distinctive as adhesion. The heat transfer coefficient seems to have some impact on the amount of cracks, the main influence though is the drying rate. For electrodes dried at $6 \text{ g m}^{-2} \text{ s}^{-1}$, critical cracking thickness slightly decreases when applying higher heat transfer coefficients, whereas the same trend is not evident for electrodes dried at higher drying rates. One explanation

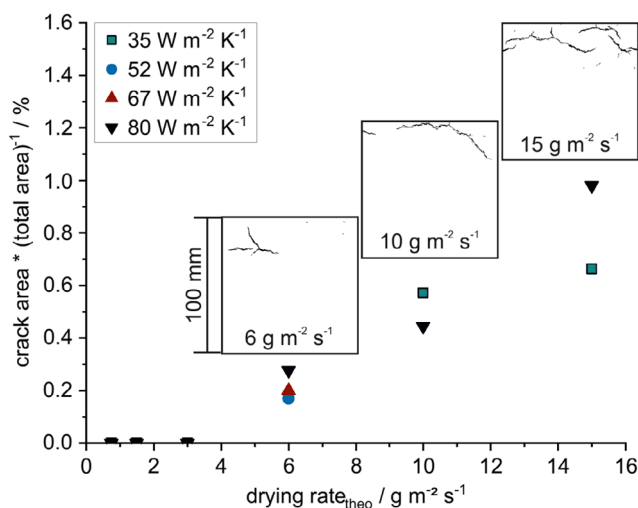


Figure 10. The percentage of crack area in relation to the whole coating area in dependency on drying conditions. All layers had an inclination of the dry electrode reaching from 89 and 512 μm .

might be the experimental setup that has a resolution of more or less $400 \mu\text{m}$ over a width of 100 mm . The slope might not only complicate attributing a defined cracking thickness to a crack position but might also lead to a slightly different drying behavior compared with flat layers. Another explanation could be that two oppositional mechanisms compete against each other here. On the one hand there is less time at higher drying rates for the particle network to relieve stress, leading to a higher probability of cracking. On the other hand, as shown in Figure 7, a larger amount of elastic SBR binder disappears from the particle-substrate interface. It might be assumed that it is transported to the electrode surface as was shown to occur with PVDF binder for NMP-based electrodes.^[16] Larger amounts of binder at the electrode surface might be able to compensate some of the stresses that developed during the drying process to a certain extent.

In summary, the experiments show that thick inclined electrodes can be dried at a drying rate of $3 \text{ g m}^{-2} \text{ s}^{-1}$ or slightly higher without cracks up to a thickness of $512 \mu\text{m}$, equaling a theoretical area capacity of 15.1 mAh cm^{-2} . These findings have been confirmed by a flat-layer coating at the same drying conditions and a thickness of $490 \mu\text{m}$, corresponding to a theoretical area capacity of 14.4 mAh cm^{-2} . Inclined coatings also hint that electrodes dried with a thickness of up to $300 \mu\text{m}$, equaling a theoretical area capacity of 8.8 mAh cm^{-2} , could be dried without cracks even at a drying rate of $15 \text{ g m}^{-2} \text{ s}^{-1}$. A crack-free coating at a drying rate of $15 \text{ g m}^{-2} \text{ s}^{-1}$ has been realized in terms of a flat coating of state-of-the-art thickness and a theoretical area capacity of 2.2 mAh cm^{-2} , whereas a limiting factor prevails in terms of binder being transported to the surface as shown in Figure 7 and a loss of adhesion.

Since cracking strongly depends on particle size distribution, additives, surface tension, as well as on rheology, the aim here is not to determine a certain critical electrode thickness at a particular drying rate but to offer possibilities to minimize or avoid cracks by means of a controlled drying process.^[14,29–34] There

is also the possibility of increasing the drying rate beyond the suggested values, when considering different drying stages of electrodes that are more or less affected by drying conditions.^[28]

When mechanical stresses are considered, one problem of electrode drying also arises when the slurry is not coated on a fixed substrate but on the flexible metal foil in a roll-to-roll-process. When the film shrinks, the foil is bent along with the dry film. This problem was not investigated in the experiments shown here. A solution might be electrodes, simultaneously coated and dried on both sides of the current collector, which should not suffer from the same effects, since identical stresses that develop during the drying step at both sides of the foil should lead to an equalization of stresses regarding the whole coating.

3. Conclusion

In conclusion, the drying process of thick electrodes—especially at industrially relevant drying rates of $1.5 \text{ g m}^{-2} \text{ s}^{-1}$ or higher—is still a challenge. It could be shown that different aspects have to be considered in that matter. First of all, during electrode drying a constant drying rate prevails even after the end of film shrinkage for all thicknesses investigated here. This means the film surface behaves like a pure water film being dried and thus has to possess water-filled surface pores during most of the drying time. This can be explained by capillary transport of the solvent to the film surface. The capillary transport does not govern the drying rate throughout the whole drying time any more when very thick electrodes are dried. In this case the thickness leads to a very complex capillary solvent network that supposedly breaks to some extent and leaves liquid clusters behind. This remaining solvent evaporates within the porous structure and therefore dries with limited mass transport and a reduced drying rate, leading to slightly prolonged process times. As an explanation as to why the binder is accumulated at the film surface during drying, capillary transport is found to be the main initiator. Additives within the solvent are dragged to the film surface along with the solvent, where they are left behind as the solvent evaporates. Experiments show a decreasing adhesion force at higher drying rates for thin and thick electrodes all the same, with an altogether lower adhesion force for thicker electrodes. This means that even though thick electrodes partly dry by solvent diffusion through the microstructure, their main drying mechanism is capillary transport, dragging binder to the surface. The different adhesion levels are explained by binder back diffusion that is hindered by an increasing length of diffusional pathways with increasing electrode thickness. A positive influence can be accomplished by processing routes using higher drying temperatures and lower heat or mass transfer coefficients to adjust certain drying rates, which is again interpreted as a consequence of back diffusion of binder. Higher temperatures might be beneficial for binder mobility, compensating its accumulation at the surface to some extent, compared with drying at the same drying rate but at a lower temperature.

As a last aspect, cracking behavior of the electrodes was investigated. Drying rate was found to actually not have an impact on the critical cracking thickness after having exceeded a critical value, though it does influence crack size. Drying rates of up

to $3 \text{ g m}^{-2} \text{ s}^{-1}$ were shown to be possible without cracking, even for electrodes six times thicker than state-of-the-art ones, though binder migration is still a problem. One solution here might be different processing routes like multilayer coatings.

In principle, drying rates of up to $15 \text{ g m}^{-2} \text{ s}^{-1}$ can be applied, resulting in crack-free coatings for state-of-the-art electrode thicknesses and even thicker, but again binder migration is the limiting factor.

4. Experimental Section

Mixing: For slurry preparation CMC (Sunrose MAC500LC, Nippon Paper industries, Japan) with a substitution degree of 0.67 was first dissolved in water at room temperature in a dissolver (Dispermat CN10, VMA Gretzmann, Germany) for 1 h. Carbon black (Super C65, Timcal, Switzerland) and graphite powder (SMGA5, Hitachi Chemical Co. Ltd., Japan) were mixed in a dry mixing step for 10 min at 200 rpm in the dissolver mixer mentioned above. Two-thirds of the dry mass were removed from the vessel and the dissolved CMC was added. The mixture was stirred for 10 min at 500 rpm and the dry mass was added in two steps. Water was added to adjust the final dry mass fraction to 43 wt%. While the temperature of the vessel was controlled by cooling water and degassing was executed, the slurry was mixed at 1500 rpm for 45 min. Before the last mixing step of 10 min at 500 rpm, SBR (Zeon Europe GmbH, Japan) was added, adding up to the dry mass composition listed in **Table 4**.

Coating and Drying: For the coating step, two different copper foils, Cu foil 1 (f1) (Nippon Foil Mfg. C., Japan) and Cu foil 2 (f2) (Schlenk Metallfolien GmbH & Co. Kg), were used as substrates. Both foils had a width of 100 mm and a thickness of $10 \mu\text{m}$. To assure a flat surface and guarantee defined drying conditions, the foil was fixed onto a temperature-controlled aluminum plate by a vacuum notch. A doctor blade (UA2000.60, Zehntner, Switzerland) was used to apply 60 mm-wide films. For coating, the substrate was moved by a stepper motor at a defined speed of 100 mm s^{-1} inside the dryer chamber. The gap width of the doctor blade was varied between 160 and $860 \mu\text{m}$.

For solvent removal, a drying chamber as described by Baunach et al. with a temperature-controlled plate and an air-nozzle dryer hub was used.^[18,23] To prevent inhomogeneous drying conditions, the heating plate was periodically moved beneath the slot nozzle array. All experiments were drying rate and not temperature controlled, though temperature influence was taken into account in separate investigations. The temperature of heating plate and gas flow at certain flow conditions and a corresponding heat transfer coefficient were adjusted to the particular day-dependent dew point, resulting in the desired drying rate, thereby accounting for seasonal changes. All experiments were conducted under isothermal drying conditions. The isothermal drying temperature equaled steady-state temperature as long as drying took place during the constant rate period, which was proven to be true for state-of-the-art thickness battery anodes and was further investigated for thicker films in this research.^[15] Drying conditions used in this research may be transferred to other dryers under knowledge of air flow conditions within the dryer, strictly speaking of heat transfer coefficient α , gas temperature, and dew point τ via **Figure 11**, which is true for water as solvent.

Table 4. Composition of the dry electrode.

Material	Dry mass [wt%]
Graphite SMGA	93
Carbon black	1.4
CMC	1.87
SBR	3.73

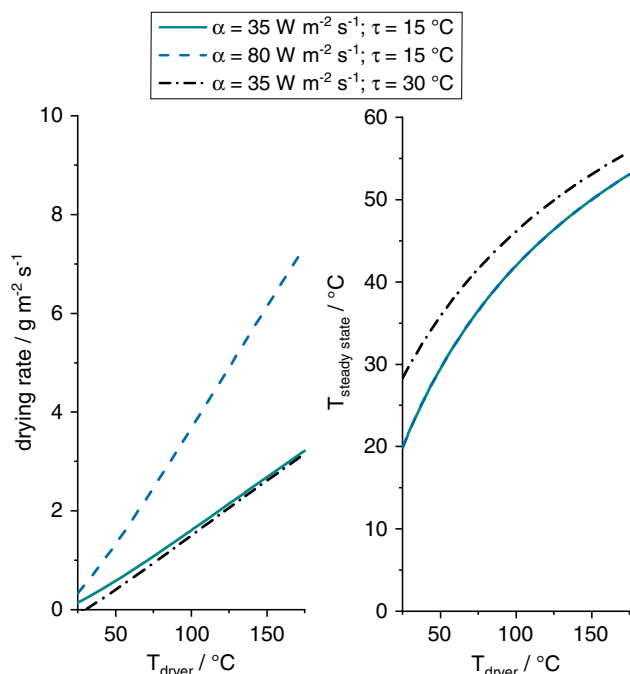


Figure 11. Correlation between drying conditions of an industrial dryer and drying rate on the left hand side as well as steady-state temperature equating isothermal drying temperature on the right hand side. Heat transfer coefficients used for simulation were 35 and 80 W m⁻² K⁻¹ and dew points were 15 and 30 °C. Calculation is valid for a one-sided coating with the same heat input from top and bottom and gas-phase kinetics.

The dependency of drying rate and steady-state temperature on gas flow temperature is shown for a heat transfer coefficient of 35 and 80 W m⁻² K⁻¹ as well as for dew points of 15 and 30 °C. For a dryer temperature of 100 °C, this would lead to a mass transfer coefficient of $\beta = 0.036 \text{ m}^2 \text{ s}^{-1}$ and $\beta = 0.081 \text{ m}^2 \text{ s}^{-1}$, respectively. As shown here, steady-state temperature at the dew point of 15 °C does not depend on air flow conditions, whereas a change in dew point to 30 °C highly affects the steady-state temperature. The influence of different dew points on the drying rate though is almost negligible, whereas the heat transfer coefficient has a strong impact. Drying conditions used in the following can be transferred by knowledge of heat transfer coefficient and dew point as exemplarily shown here.

Annealing: To investigate the influence of an annealing step after the drying step, samples were put between two metal plates to avoid bending and ensure a homogenous heat input. These samples were put into a preheated vacuum furnace for 10 min at 10 mbar and at different temperatures, as shown in Figure 6.

Drying Curves: Drying curves were determined by means of residual moisture measurements: Slurries were coated with a certain thickness and dried under defined conditions. The drying process was interrupted at precise time intervals during drying and a sample was taken and directly weighed. The procedure was repeated several times with differing interruption time intervals until a drying curve was derived.

Cracking Experiments: For determination of critical cracking thickness, samples were coated and dried as described in the Coating and Drying section. In contrast to the usual setup though, the doctor blade was 100 mm in width and not adjusted with two identical gaps on the left and right side but with a gap of 160 μm at one side and 1000 μm at the other side.

The thickness of each coated layer was measured perpendicular to the coating direction over the whole coating width at least at two different positions, where no cracks occurred if possible. A linear fit was used to

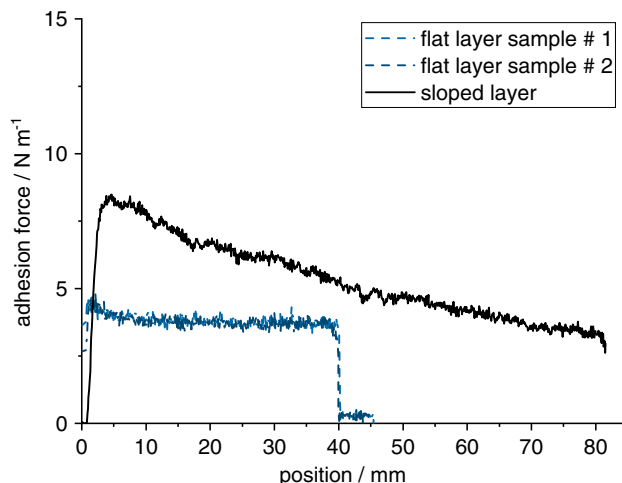


Figure 12. Exemplary results of single adhesion force measurements for two flat layers and a sloped layer.

correlate position and thickness of each layer. All coated layers were scanned on a flat-bed scanner. In a further step all images were processed in “ImageJ.” After converting them to 8-bit pictures the software tool “Find Edges” was used to differentiate between crack-free coatings and cracks. The total area of each picture was determined, averaging $40270 \pm 497 \text{ mm}^2$. The crack area of each picture was analyzed by the software tool “analyse particles” whereas all areas smaller than 0.3 mm² were excluded. Each crack reaching into the coating was considered for evaluation of a critical cracking thickness. For each crack, the position reaching farthest into the coating was determined and correlated with thickness, resulting in critical cracking thickness.

Adhesion Measurements: Before adhesion measurements were conducted, samples were stored within a vacuum furnace for 48 h at 10 mbar and 30 °C. Adhesion force was measured using a universal testing machine (AMETEK LS1) with a 90° peel test device and a 10 N load cell. Samples of 30 mm width were cut perpendicular to the coating direction with six samples per coating. With a 90° peel test, measurements can be conducted perpendicular to the coating direction with a good resolution. In Figure 12, two exemplary measurements for flat layers are shown, which are in good agreement regarding repeatability.

Furthermore, a sloped layer was measured with a coating thickness reaching from 89 to 512 μm. Evidently, the measuring technique is advantageous regarding observations of coating and drying inhomogeneities.

Acknowledgements

The authors acknowledge the financial support of the Federal Ministry of Education and Research (BMBF) within the cluster project “ProZell High Energy” under the reference number 03XP0073B. This work contributes to the research performed at Center for Electrochemical Energy Storage Ulm-Karlsruhe (CELEST). ZEISS MERLIN SEM was financially supported by the Federal Ministry of Economics and Technology on the basis of a decision by the German Bundestag within the BMBF grant number 03ET6017. The authors would also like to thank the students involved in this work: J. Knack and A. Albrecht. Open access funding enabled and organized by Projekt DEAL.

Conflict of Interest

The authors declare no conflict of interest.

Keywords

binder migration, drying, film formation, lithium-ion batteries, thick anodes

Received: June 18, 2019

Revised: August 30, 2019

Published online: September 25, 2019

-
- [1] Roland Berger GmbH, *E-mobility Index 2018: Study*, Roland Berger GmbH, Munich, Germany **2018**.
- [2] G. Patry, A. Romagny, S. Martinet, D. Froelich, *Energy Sci. Eng.* **2015**, 3, 71.
- [3] D. L. Wood, J. Li, C. Daniel, *J. Power Sources* **2015**, 275, 234.
- [4] M. Singh, J. Kaiser, H. Hahn, *J. Electrochem. Soc.* **2015**, 162, A1196.
- [5] M. Singh, J. Kaiser, H. Hahn, *J. Electroanal. Chem.* **2016**, 782, 245.
- [6] H. Zheng, J. Li, X. Song, G. Liu, V. S. Battaglia, *Electrochim. Acta* **2012**, 71, 258.
- [7] T. Danner, M. Singh, S. Hein, J. Kaiser, H. Hahn, A. Latz, *J. Power Sources* **2016**, 334, 191.
- [8] W. Pfleging, *Nanophotonics* **2018**, 7, 549.
- [9] P. Smyrek, J. Pröll, H. J. Seifert, W. Pfleging, *J. Electrochem. Soc.* **2015**, 163, A19.
- [10] M. A. Ghadkolai, S. Creager, J. Nanda, R. K. Bordia, *J. Electrochem. Soc.* **2017**, 164, A2603.
- [11] J. S. Sander, R. M. Erb, L. Li, A. Gurijala, Y.-M. Chiang, *Nat Energy* **2016**, 1, 3828.
- [12] C.-J. Bae, C. K. Erdonmez, J. W. Halloran, Y.-M. Chiang, *Adv. Mater.* **2013**, 25, 1254.
- [13] Z. Du, D. L. Wood, C. Daniel, S. Kalnaus, J. Li, *J Appl Electrochem.* **2017**, 47, 405.
- [14] B.-S. Lee, Z. Wu, V. Petrova, X. Xing, H.-D. Lim, H. Liu, P. Liu, *J. Electrochem. Soc.* **2018**, 165, A525.
- [15] S. Jaiser, M. Müller, M. Baunach, W. Bauer, P. Scharfer, W. Schabel, *J. Power Sources* **2016**, 318, 210.
- [16] S. Jaiser, J. Kumberg, J. Klaver, J. L. Urai, W. Schabel, J. Schmatz, P. Scharfer, *J. Power Sources* **2017**, 345, 97.
- [17] Verein Deutscher Ingenieure, *VDI Heat Atlas*, 2nd ed., VDI-Buch, Springer-Verlag, Berlin, Heidelberg **2010**.
- [18] M. Baunach, S. Jaiser, P. Cavadini, P. Scharfer, W. Schabel, *J. Coat. Technol. Res.* **2015**, 12, 915.
- [19] E.-U. Schlünder, *Chem. Ing. Tech.* **1988**, 60, 117.
- [20] E.-U. Schlünder, *Dry. Technol.* **2004**, 22, 1517.
- [21] J. M. P. Q. Delgado, G. B. A. de Lima, *Drying and Energy Technologies*, Advanced Structured Materials, Springer, Cham **2016**.
- [22] L. Pfaffmann, S. Jaiser, M. Müller, P. Scharfer, W. Schabel, W. Bauer, F. Scheiba, H. Ehrenberg, *J. Power Sources* **2017**, 363, 460.
- [23] M. Baunach, S. Jaiser, S. Schmelzle, H. Nirschl, P. Scharfer, W. Schabel, *Dry. Technol.* **2015**, 34, 462.
- [24] M. Baunach, M. Müller, S. Jaiser, W. Bauer, P. Scharfer, W. Schabel, unpublished.
- [25] R. Morasch, J. Landesfeind, B. Suthar, H. A. Gasteiger, *J. Electrochem. Soc.* **2018**, 165, A3459.
- [26] F. Font, B. Protas, G. Richardson, J. M. Foster, *J. Power Sources* **2018**, 393, S. 177.
- [27] M. Müller, L. Pfaffmann, S. Jaiser, M. Baunach, V. Trouillet, F. Scheiba, P. Scharfer, W. Schabel, W. Bauer, *J. Power Sources* **2017**, 340, 20171.
- [28] S. Jaiser, A. Friske, M. Baunach, P. Scharfer, W. Schabel, *Dry. Technol.* **2016**, 35, 1266.
- [29] H. N. Yow, M. Goikoetxea, L. Goehring, A. F. Routh, *J. Colloid Interface Sci.* **2010**, 352, 542.
- [30] W. P. Lee, A. F. Routh, *Langmuir* **2004**, 20, 9885.
- [31] E. Santanach Carreras, F. Chabert, D. E. Dunstan, G. V. Franks, *J. Colloid Interface Sci.* **2007**, 313, 160.
- [32] S. Lim, S. Kim, K. H. Ahn, S. J. Lee, *Ind. Eng. Chem. Res.* **2015**, 54, 6146.
- [33] H. Zheng, L. Zhang, G. Liu, X. Song, V. S. Battaglia, *J. Power Sources* **2012**, 217, 530.
- [34] Z. Du, K. M. Rollag, J. Li, S. J. An, M. Wood, Y. Sheng, P. P. Mukherjee, C. Daniel, D. L. Wood, *J. Power Sources* **2017**, 354, 200.